ACS OMEGA

Open Access

This article is licensed under CC-BY-NC-ND 4.0

http://pubs.acs.org/journal/acsodf

Article

Microwave-Fluidic Continuous Manufacturing of Ultrasmall Silver Nanoparticles in a Polycaprolactone Matrix as Antibacterial Coatings

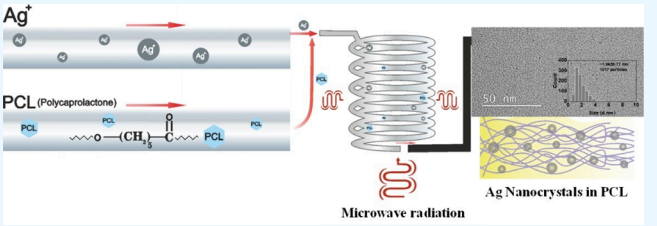
Mona Nejatpour, Oğuz Bayındır, Pelin Duru, Milad Torabfam, Cem Meriç, Hasan Kurt, Meral Yüce, and Mustafa Kemal Bayazıt*

Cite This: *ACS Omega* 2025, 10, 18213−18224

Read Online

ACCESS | Metrics & More | Article Recommendations | Supporting Information

ABSTRACT: Fast, energy-efficient, and continuous manufacturing of nanoparticles (NPs) with controlled size and distribution in polymer matrices is challenging. Herein, a microwave-powered dual-injection continuous flow reactor is presented to prepare silver NP (AgNP)/polycaprolactone (PCL) nanocomposites (AgNP/PCL NCs). Ultrasmall spherical AgNPs (US-AgNPs, 1.86 ± 0.77 nm) can be manufactured in the PCL matrix in less than 3 min at ∼35 °C by applying 60 W microwave power and a combined flow rate of 1.25:1.25 mL/min (Pump1:Pump2). The effect of NP size and amount on the thermal, optical, and antimicrobial properties and the crystallinity of NCs are discussed. The NC crystallinity is independent of the NP's size and amount, while the NC film roughness is highly dependent on NP size. The antibacterial activity of the US-AgNPs-containing NC toward *Escherichia coli* (∼98.2%), *Pseudomonas aeruginosa* (∼98.2%), and *Staphylococcus aureus* (∼99.1%) is higher than big AgNP-containing NCs (82.3%, 85.7%, and 92.3%, respectively), signifying a strong NP size dependency instead of Ag concentration.



INTRODUCTION

In the early 20th century, infectious diseases were the main reason for worldwide deaths, and antibiotics were used as an antimicrobial weapon to fight against contagious diseases.[1] The overuse and misuse of antibiotics have led to the emergence of antibiotic-resistant bacteria, a primary global health concern; thus, addressing antibiotic resistance is a key challenge, and developing alternative combatting approaches for the bacteria is highly envisaged. Inorganic nanoparticles (NPs) like silver (Ag), gold (Au), copper (Cu), copper oxide (CuO), and zinc oxide (ZnO) NPs have been considered viable antimicrobial alternatives in various fields, including the food industry, medicine, water filtration, and textiles.[2−6] They can be instrumental in combating antimicrobial and antibiotic resistance if fine control over their usage, including minimum inhibitory concentration, size, and distribution, is achieved. Among the NPs, particularly AgNPs, promising nondrug antimicrobial agents have attracted particular attention because of their lethal effect on many Gram-positive/negative bacteria and pathogens.[7] The antibacterial effect of AgNPs depends on their size, morphology, dispersion, and coating quality, in which aggregation of AgNPs reduces the antibacterial effect.[7−11] AgNP/Polymer nanocomposites (NCs), providing an effective alternative to metallic AgNPs alone, are frequently used as antibacterial agents in various polymer-based applications. By manipulating the size and morphology of NPs within a polymer matrix, NCs can be formed and utilized as films and fibers. However, the main challenges in their applications are continuously preparing NCs without NP agglomeration, maintaining homogeneous NP distribution and size control in a polymer matrix, and the ability for coating, which affects the NC antibacterial efficiency, mechanical properties, polymer chain conformation, and mobility.[12,13]

Additionally, incorporating hydrophobic polymers can create anchoring sites for bacteria, resulting in greater antibacterial efficiency.[2,8,9,14] Polycaprolactone (PCL) is one of the common hydrophobic polymers with a wide range of applications in drug delivery, sutures, long-term implants, wound dressing materials, scaffolds for tissue engineering, packaging, textiles, and membranes for water treatment due to its biocompatibility, slow biodegradation time arising from its high hydrophobicity, and thermal stability.[15−20]

Hydrophobic polymers like PCL enhance antibacterial efficiency by creating a barrier that significantly limits bacterial colonization. This is due to their inherent water-repellent nature, which makes it difficult for bacteria to adhere to

Received: April 15, 2024
Revised: June 24, 2024
Accepted: June 26, 2024
Published: May 1, 2025



© 2025 The Authors. Published by American Chemical Society

Downloaded from pubs.acs.org/acsodf/article-pdf/10/18/18213/4082497/5/ao4c03612.pdf by guest on 26 October 2026

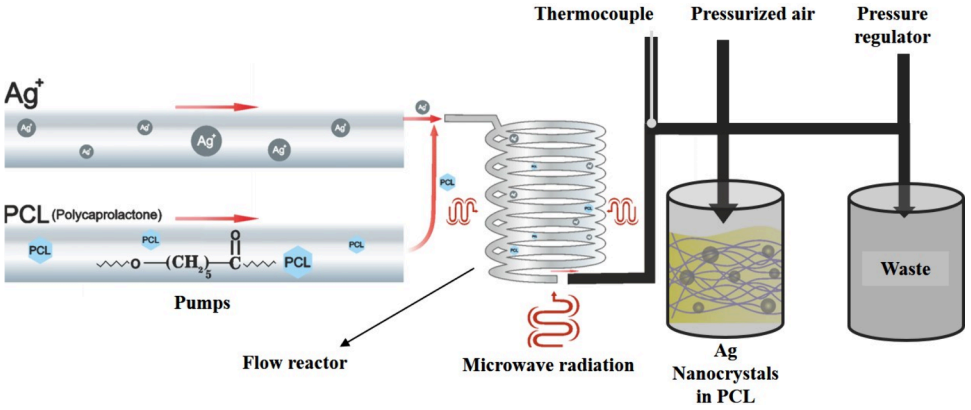


Figure 1. Illustration of a double-pump continuous MWFS to prepare NCs.

hydrophobic surfaces. Unlike hydrophilic polymers, which can form a hydration layer that facilitates bacterial attachment, hydrophobic polymers exhibit low surface energies and repel water. This characteristic prevents water-based microbial solutions, such as bacterial biofilms, from establishing a foothold on the surface. Embedding AgNPs within the PCL matrix stabilizes them, preventing aggregation and ensuring a more uniform distribution. It also allows for controlled and sustained release of AgNPs, enhancing their antibacterial efficacy.[21−23] Meanwhile, AgNP/PCL NCs' surface modifications can enhance their interaction with biological tissues, improving cell adhesion and proliferation.[24,25]

There are few works on synthesizing AgNPs/PCL NCs and their antibacterial properties.[2,19,26,27] For example, AgNP/PCL/PEG NC were fabricated using an in situ reduction method of Ag salt in different concentrations inside the PCL/PEG matrix, and a decrease in *S. aureus* bacteria was reported on the site of NCs.[2] Results underscored that the amount of AgNPs with a broad size distribution of ∼2−20 nm did not affect the antibacterial effectiveness of NCs against *S. aureus* bacteria. However, AgNP concentration dependency was reported for *P. aeruginosa* bacteria. 3D printed AgNP/PCL NC scaffolds, prepared by in situ reduction of Ag salts to 20−150 nm AgNPs in the PCL matrix as antibacterial tissue, effectively decreased *E. coli* concentration.[27] A AgNPs/PCL/poly(ethylene oxide) nanofiber scaffold was also prepared via the ex situ blending of AgNP (15.4 ± 3.66 nm) and used as an antibacterial mat for wound healing applications.[19] Although the above-described studies have advantages, continuous manufacturing of US-AgNPs (<5 nm) with a narrow size distribution in the PCL matrix is a long-lasting challenge. Thus, developing novel manufacturing strategies is still required. In addition, potentially scalable polymer NC manufacturing processes are globally critical in the fast-growing polymer NC industry.

Synthesizing NPs using microwave heating in a batch reactor is a well-practiced, eco-friendly method offering a scale-up potential because of its short reaction time, high purity, high yield, and low energy cost.[28] However, there are several difficulties, such as the limited penetration depth of the microwave radiation and the reactor size while scaling up batch synthesis.[29] Nevertheless, when microwave heating is coupled with the flow reactors, it offers a scalable synthesis opportunity.[30−34] Furthermore, it mitigates the safety concerns regarding overheating large reactors under continuous microwave heating conditions.

In our group, a recent proof-of-concept study reported that a microwave-fluidic system (MWFS) was highly suitable for manufacturing nylon-6 NCs bearing evenly distributed AgNPs with a mean size of ∼2.59 ± 0.64 nm in ∼2 min at ∼50−55 °C using the green solvent formic acid (FA) and reducing agent $NaBH_4$.[35] We also showed the potential of continuous microwave-fluidic reactors to manufacture homogeneously distributed AgNPs (∼5 nm) in a thermoplastic polyurethane matrix without any reducing agent at ∼40 °C in approximately 4 min.[36]

Herein, continuous manufacturing of US-AgNPs (1.86 ± 0.77 nm by transmission electron microscopy (TEM)) in a biodegradable polymer matrix, PCL, in less than 3 min at ∼35 °C under microwave-fluidic conditions without a reducing agent is presented. The NP size control in the PCL matrix is achieved by fine-tuning the microwave power (MWP), flow rate, and $AgNO_3$ and PCL concentrations. The effect of the AgNP size on PCL's thermal, optical, and crystal properties is discussed. Furthermore, the size-dependent antibacterial activity of the prepared NC films on *S.* aureus, *P. aeruginosa*, and *E. coli* bacteria is assessed as potential biodegradable, antibacterial hybrid materials that are potentially convenient for biomedicine, packaging, and textile applications. This study introduces a continuous energy-efficient and green process, bringing a novel viewpoint to traditional polymer-based nanocomposite manufacturing and offering control over the filler's size and distribution. It further fills a crucial knowledge gap by demonstrating that the antibacterial efficacy of these NCs is predominantly influenced by AgNP size rather than concentration, highlighting the importance of precise NP control for advanced antimicrobial applications. Our findings pave the way for more efficient and scalable production techniques in NC fabrication.

MATERIAL AND METHODS

Materials. Silver nitrate ($AgNO_3$, ISOLAB, ≥99.8%), polycaprolactone (PCL, $(C_6H_{10}O_2)_n$, Mw: 8000, Sigma-Aldrich), *N*,*N*-dimethylformamide (DMF, ≥99%, ISOLAB), dimethyl sulfoxide (DMSO, ≥99.9%, ISOLAB), and sulfuric acid (95−98%, ISOLAB) were used without further purification.

AgNP/PCL NC Manufacturing. The designed MWFS used in synthesizing NCs is illustrated in Figure 1. It is composed of several key components for efficient and controlled reactions. Central to the system is a custom-designed fluidic reactor constructed from microwave-trans-

Downloaded from pubs.acs.org/acsodf/article-pdf/10/18/18213/4082497/5/ao4c03612.pdf by guest on 26 October 2026

https://doi.org/10.1021/acsomega.4c03612
ACS Omega 2025, 10, 18213−18224

Table 1. Critical Experimental Parameters (e.g., Precursor Concentrations, MWPs, Flow Rates) and Some Essential Experimental Data (e.g., Temperature, Absorption Maxima, Particle Size, and Its Distribution) for NC1-16

AgNP/PCL NC	$AgNO_3$ conc. in DMSO(mg/mL)	PCL conc. in DMF(mg/mL)	Flow rates ($AgNO_3$: PCL) (mL/min)	MW power (W)	Temperature outside the reactor exit (°C) ± 2	UV−vis λ_{max} (nm)	fwhm	DLS HD size (nm)	PDI
1	0.10	10	(0.50:0.50)	70	36.3	~448, ~737$_{fwhm}$	~467	27.46 ± 1.39	~0.28
2	0.10	10	(0.75:0.75)	70	26.2	~450, ~687$_{fwhm}$	~457	5.34 ± 0.17	~0.14
3	0.10	10	(0.75:0.75)	60	42.8	~434	~263	5.37 ± 0.29	~0.10
4	0.10	10	(0.75:0.75)	50	54.6	~429	~211	4.45 ± 0.44	~0.55
5	0.10	10	(0.75:0.75)	40	40.0	~433	~206	6.65 ± 0.28	~0.17
6	0.10	10	(0.75:0.75)	30	37.3	~434	~216	4.83 ± 0.64	~0.26
7	0.10	10	(1.50:1.50)	60	36.0	~429	~208	2.26 ± 0.15	~0.31
8	0.10	10	(1.25:1.25)	60	35.3	~428	~218	2.43 ± 0.62	~0.10
9	0.10	10	(1.00:1.00)	60	35.5	~440	~261	3.24 ± 0.03	~0.22
10	0.10	10	(0.50:0.50)	60	37.5	~454, ~734$_{fwhm}$	~474	53.84 ± 0.98	~0.41
11	0.10	10	(0.25:0.25)	60	38.0	~436, ~767$_{fwhm}$	~484	55.99 ± 4.79	~0.49
12	0.20	10	(1.00:1.00)	60	41.2	~436	~223	3.17 ± 0.65	~0.66
13	0.05	10	(1.00:1.00)	60	37.6	~436	~194	2.253 ± 0.043	~0.40
14	0.02	10	(1.00:1.00)	60	36.6	~429	~239	1.933 ± 0.242	~0.20
15	0.10	5	(1.00:1.00)	60	52.0	~426, ~673$_{fwhm}$	~426	8.819 ± 0.029	~0.44
16	0.10	20	(1.00:1.00)	60	53.3	~411	~271	3.002 ± 0.221	~0.57

parent Teflon tubing (o.d. 3.175 mm and i.d. 2 mm) coiled around a PTFE cylinder with a diameter of 5.5 cm and a volume of 6.6 mL. A single-mode commercial TE10 microwave system ((Discover, CEM Corp., USA)), operating at 2.45 GHz, is the primary power source with a real-time computer system using the in-built Synergy software. Temperature regulation is achieved through a dedicated Omega HH801B digital thermometer equipped with a compact transition joint probe (Omega, WNW0187979) (Omega Engineering, Inc., Stamford, CT, USA), strategically positioned 11 cm from the microwave heating zone. A 20 psi pressure regulator (IDEX Health and Science) is utilized to maintain the internal system pressure. The system's fluid delivery mechanism is facilitated by a Gemini 88 Plus dual rate syringe pump (KD Scientific Inc., Holliston, MA, USA), using two 60 mL syringes (Luer-Lock) for fluid injection. The setup includes product and waste collection provisions, with separate glass bottles designated for each. In a typical synthesis, $AgNO_3$ and PCL dissolved in DMSO and DMF at different concentrations are pumped through the flow reactor under applied MWPs (Table 1). Sixteen different AgNP/PCL NCs (NC1−16) were prepared to study the MWP, flow rate, and $AgNO_3$ and PCL concentration effects on the NP size, morphology, and antibacterial effects (Table 1).

The AgNP/PCL NC solutions were mixed with ethanol (v/v 1:1), and precipitation occurred in 5 min. The precipitated AgNP/PCL NC was filtered using PTFE membranes (0.22 μm pore size). The solid AgNP/PCL NC was redispersed in ethanol, filtered, and rinsed by ethanol. This process was repeated three times to ensure the complete removal of DMF and DMSO. The filtered AgNP/PCL NCs were placed in a desiccator for 2 days for drying and used for other characterizations. The photographs of the dry NC powders are in SI Figure S1.

The NC films were fabricated using fresh samples after synthesis via a dip coating method utilizing the HOLMARC HO-TH-01T, India Dip Coating Equipment. Glass substrates were submerged into the NC solution at a controlled speed of 200 μL/min, ensuring uniform coating, and subsequently retrieved at the same speed. A waiting period of 1 min was applied at the dipping and retrieval positions to allow for proper film formation.

Antibacterial Test Method. The antibacterial properties of Ag NPs/PCL NCs were evaluated using the Japanese Industrial Standard (JIS) method (JIS Z2801:2010) (JSA, 2000), a procedure that is highly sensitive to antimicrobial activity and also applicable in various real-world fields such as hospitals and clinics, which focused on preventing the growth of bacteria on the products. A graphical demonstration of this method is given in SI Figure S2. Two Gram-negative bacteria, *P. aeruginosa* and *E. coli*, and one Gram-positive bacteria, *S. aureus*, were chosen for this evaluation. The bacteria selection was made considering PCL application areas. As a first step, bacteria from a single colony of 5 mL of Lysogeny broth (LB) were inoculated and incubated overnight at 37 °C. Second, a dilution process was performed to obtain the target bacteria number of 1.5×10^8 colony-forming units (CFU)/mL to ensure a standard bacterial load for reliable and constant efficiency of antimicrobial evaluation in our assay. Then, the diluted sample was utilized for further assessment. Two Gram-negative bacteria, *P. aeruginosa* and *E. coli*, and one Gram-positive bacteria, *S. aureus*, were chosen for this evaluation. The bacteria selection was made considering PCL application areas. Regarding each of these three bacteria, glasses of 12 × 12 mm were provided and divided into two groups, uncovered (control) and AgNP/PCL NC covered. Then, for sterilization of the glasses, all were located in a hood with laminar flow to ensure a clean environment that is free from contaminants, followed by exposure to ultraviolet radiation to eliminate any

Downloaded from pubs.acs.org/acsodf/article-pdf/10/18/18213/4082497/ao4c03612.pdf by guest on 26 October 2026

https://doi.org/10.1021/acsomega.4c03612
ACS Omega 2025, 10, 18213−18224

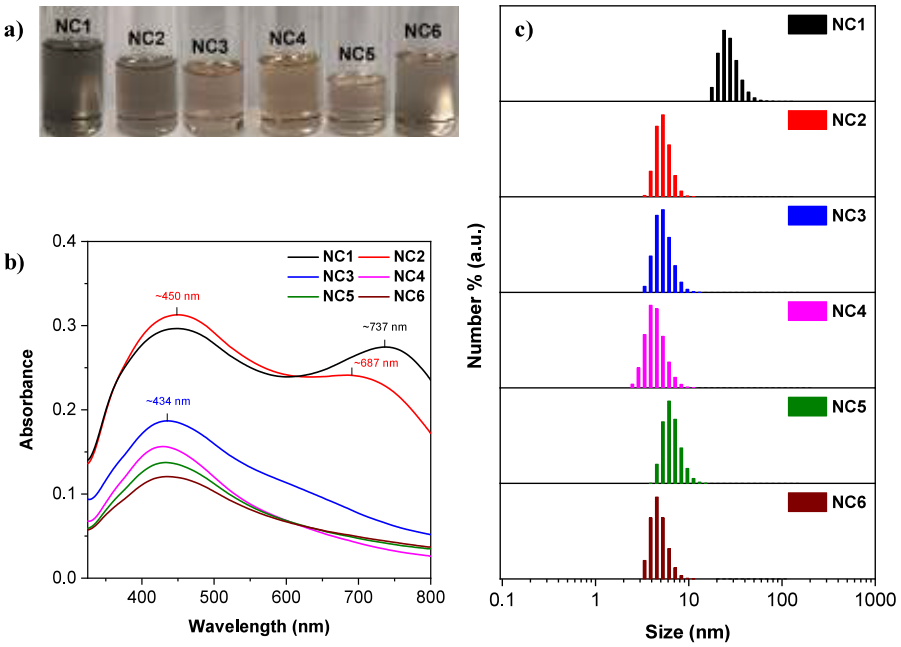


Figure 2. Effect of MW power. a) Photographs of as-prepared NC1−6 solutions, b) UV−vis spectra, and c) particle size analysis (by DLS) of NC1−6.

possible remaining microorganisms, resulting in efficient sterilization.

Furthermore, 25 μL of culture medium containing target bacteria was transferred on covered and uncovered glasses. The separate Petri dishes with the lid closed were used on which to put the glasses. The overnight incubation step at 37 °C was followed by putting samples in tubes and washing them with 10 mL of phosphate-buffered saline (PBS) to guarantee the effective transfer of bacteria from glass to the PBS solution. Following this, the dilution process was performed, in which 1 mL of the solution was poured into the next tube containing 9 mL of PBS. This step was repeated to achieve 6-fold serial dilutions and obtain a lower concentration, which provides the countable resulting bacterial colonies and enables precise assessments. All steps were performed on both uncovered and covered glasses, which is noteworthy. To give sufficient time for bacteria growth, 1 mL from the final solution diluted in the previous step was spread all over the Petri dish containing nutrient broth and placed in an incubator at 37 °C for 24 h. For the calculation of antibacterial rate, eq 1 based on the JIS Z2801:2010 regulation was used.[37]

$$\text{Antibacterial rate } (\%) = \frac{Nu - Nc}{Nu} \quad (1)$$

In this formula, *Nu* and *Nc* represent the number of viable bacteria on uncoated glass and those on covered glass after incubation for 24 h.

Characterization. Ultraviolet−visible (UV−vis) absorption spectroscopy was conducted on AgNP/PCL NCs immediately after synthesis using a double-beam UV/vis-NIR spectrophotometer (Varian Cary 5000 UV/vis-NIR spectrometer, Varian Australia Pty Ltd., Australia) in the spectral range of 200 to 800 nm. The UV−vis absorbance spectra's full width at half-maximum (fwhm) value was calculated using Origin Lab software. Dynamic light scattering (DLS) was performed to measure the dynamic size of the AgNPs using a Malvern ZetaSizer Nano (Malvern Panalytical Ltd., Worcestershire, UK). For DLS measurements, AgNP/PCL NCs were diluted by DMF in the ratio of 1:10 with a final concentration of 1 mg/mL of the samples and were filtered through a PTFE membrane of 0.22 μm pore size (ISOLAB). High-resolution transmission electron microscopy (HRTEM) images were acquired using a JEOL JEM ARM200CF (Tokyo, Japan), operated at 200 kV, and immediately after synthesis, 20 μL of the sample was loaded onto carbon-coated TEM grids and dried overnight. FTIR analysis (attenuated total reflection (ATR)) of the dried samples was carried out by a Thermo Scientific Nicolet iS10 (USA) between 525 and 4000 cm^{-1}. X-ray diffraction (XRD) analysis was conducted by a D2 and D8 (only for NC15 and NC16) Phaser diffractometer (Bruker, Billerica, MA, USA) using Cu Kα radiation. This measurement's 2θ range and step size were chosen as 5−90° and 0.01, respectively. Thermal properties of pure PCL and selected AgNP/PCL NCs were studied using thermal gravimetric analysis (TGA) and differential thermal analysis (DTA). TGA-DTA measurements were performed using a Shimadzu DTG 60H. All samples were heated from 10 to 1000 °C with a heating rate of 10 °C/min under an airflow rate of 100 mL/min. Optical properties of AgNP/PCL NC films were determined by an M2000 ellipsometer (J.A. Woollam Co. Inc., Lincoln, NE, USA) at 60°, 65°, 70°, and 75° angles of the incident for a wavelength of 400−900 nm. The thickness of the nanocomposite and pure PCL thin films and the refractive index and extinction coefficient dispersion curves of the thin films were obtained by optical modeling of the obtained curves using the Cauchy equation, as shown in eq 2.[38]

$$n(\lambda) = A + \frac{B}{\lambda^2} + \frac{C}{\lambda^4} \quad (2)$$

where *n* denotes the refractive index, λ is the wavelength of light, and *A*, *B*, and *C* are material-dependent constants referred to as Cauchy constants.

Analysis was conducted using inductively coupled plasma-optical emission spectrometry (ICP-OES, Varian, Australia) to

Downloaded from pubs.acs.org/acsodf/article-pdf/10/18/18213/4082497/5/ao4c03612.pdf by guest on 26 October 2026

https://doi.org/10.1021/acsomega.4c03612
ACS Omega 2025, 10, 18213−18224

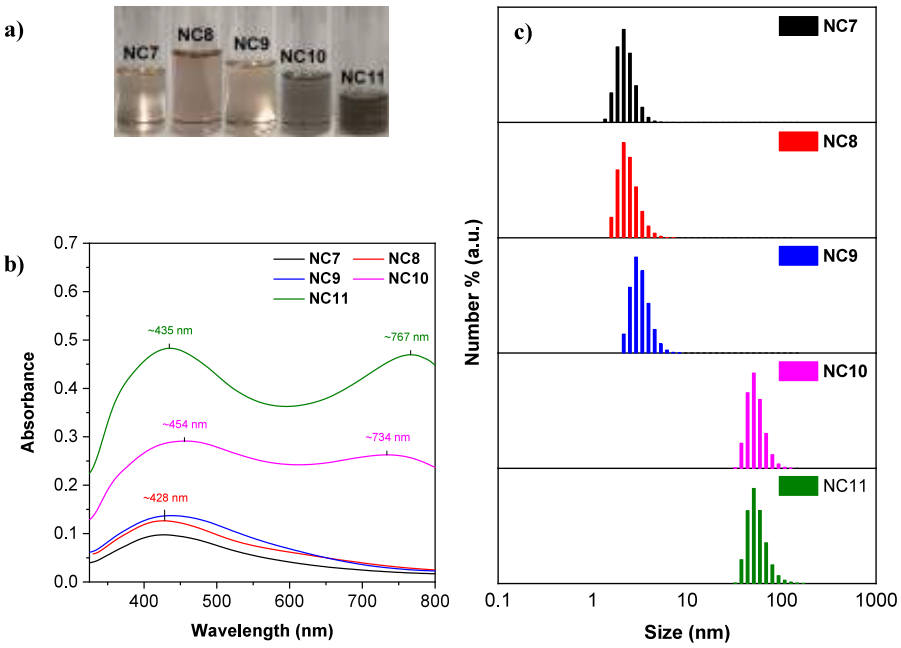


Figure 3. Effect of flow rate. a) Photographs of as-prepared NC7−11 solutions, b) UV−vis spectra, and c) particle size analysis (by DLS) of NC7−11.

determine the quantity of AgNPs present in NC8 and NC11, which were utilized for antibacterial assessments. Briefly, 10 mg of dried NC was combined with 5 mL of sulfuric acid, then subjected to a 5 min heating process at 200 °C using a single-mode microwave system (Discover, CEM Microwave Technology Ltd.) operating at 200 W. Following this, the dissolved samples were diluted in DI water to reach a total volume of 20 mL and filtered through a PTFE membrane with a pore size of 0.22 μm (ISOLAB) before analysis.

RESULTS AND DISCUSSIONS

AgNP-containing PCL NCs (NC1 to NC16) were prepared continuously in a solvent mixture (DMSO/DMF) using the dual-pump MWFS shown in Figure 1. DMF can reduce Ag^+ even at room temperature,[39,40] while DMSO has no such reducing effect.[36] The reduction can be further accelerated by the MW. A possible reaction between DMF and Ag^+ can be[41]

$$HCONMe_2 + 2Ag^+ + H_2O \rightarrow 2Ag^0 + Me_2NCOOH + 2H^+$$

The experimental parameters affecting the AgNP size, morphology, and distribution in the PCL matrix (e.g., precursor concentration, MWP, and flow rate) were studied systematically. AgNP formation in the PCL matrix was monitored using UV−vis spectroscopy, and the fwhm's were calculated using corresponding UV−vis spectra. DLS was employed to assess the hydrodynamic size (HD) and polydispersity index (PDI) of AgNPs in the PCL matrix. The results are tabulated in Table 1.

Transparent AgNP/PCL NC solutions were obtained for all manufactured NCs (NC1−6) under the applied MWPs of 30, 40, 50, 60, and 70 W, and the solution color changed from pale yellow to gray when the MWP increased (Figure 2a) (from 30 to 70 W). The absorption spectra of NC1 and NC2 prepared under 70 W displayed two absorption maxima (λ_{max}) at ca. 450 and 700 nm (Figure 2b). Such absorption profiles can be attributed to high-aspect-ratio rod-like AgNPs with the transverse (high energy) and longitudinal (low energy) plasmon resonance due to the shape anisotropy.[42]

Under 70 W, when the combined flow rate changed from 0.50:0.50 mL/min (NC1) to 0.75:0.75 mL/min (NC2), in other words, when the MW exposure time decreased, there was almost no change in the position of the transverse plasmon resonance (TPR) ($\sim 448_{NC1}$ nm vs 450_{NC2} nm); however, the longitudinal plasmon resonance (LPR) for NC2 blue-shifted by ∼50 nm to ∼697 nm compared to ∼737 nm for NC1 (Figure 2b). In the literature, the blue-shift in the LPR peak is attributed to a decrease in the aspect ratio of Ag nanorods.[42] Considering that the DLS mean particle sizes of NC1 and NC2 are 27.46 ± 1.39 nm and 5.34 ± 0.17 nm, respectively (Figure 2c), one can suggest that the low-aspect-ratio and small rod-like AgNPs are produced in the MWFS when the flow rate increased at constant MWP and precursor concentrations. Furthermore, the fwhm values of $NC1_{LPR}$ and $NC2_{LPR}$ were comparable ($\sim 467_{NC1}$ nm vs 457_{NC2} nm); however, the polydispersity in NC1 (PDI ∼ 0.28) was higher than that in NC2 (PDI ∼ 0.14), suggesting a variation in particle sizes under a flow regime of 0.50:0.50 mL/min (Table 1). Such an observed change in the size and aspect ratio of AgNPs can be ascribed to the MW exposure time, which drives the particle growth at increased reaction times. However, under the same flow rates (0.50:0.50 mL/min) using MWP intensities lower than 70 W (e.g., 50 W (NC4), 40 W (NC5), 30 W (NC6)), UV−vis analysis suggests the formation of spherical NPs (Figure 2b). Furthermore, no LPR peak is observed, revealing a strong correlation between the rod-like AgNP formation in an MWFS and the applied MWP intensity. The weak absorption band above ∼600 nm in the UV−vis spectrum of NC3 hints at a few nonspherical NPs at 60 W under the flow rate of 0.50:0.50 mL/min. The DLS-based mean particle sizes and the λ_{max} values of AgNPs in NC3−6 were comparable (Figure 2c and Table 1); however, their absorbance intensities

Downloaded from pubs.acs.org/acsodf/article-pdf/10/18/18213/4082497/5/ao4c03612.pdf by guest on 26 October 2026

https://doi.org/10.1021/acsomega.4c03612
ACS Omega 2025, 10, 18213−18224

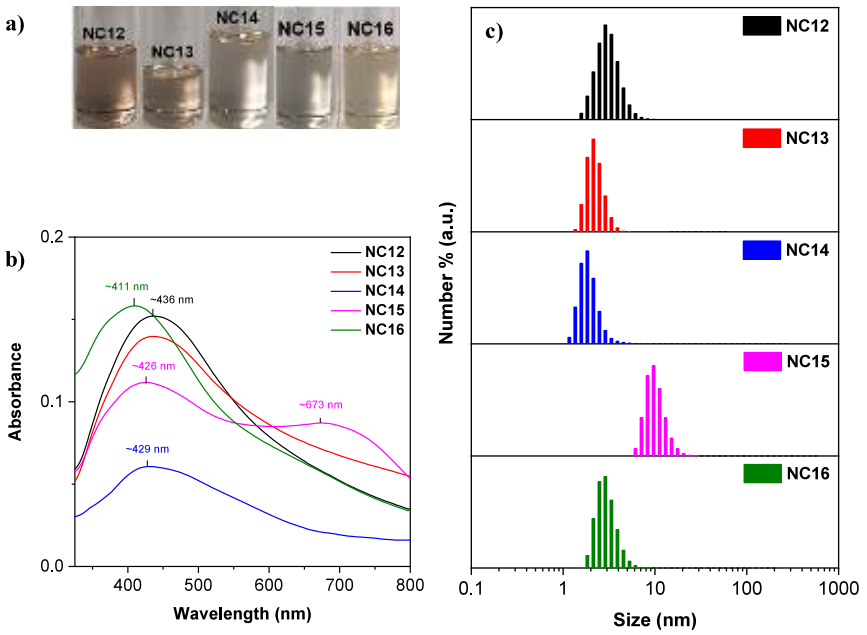


Figure 4. Effect of $AgNO_3$ and PCL concentrations. a) Photographs of as-prepared NC12−16 solutions, b) UV−vis spectra, and c) particle size analysis (by DLS) of NC12−16.

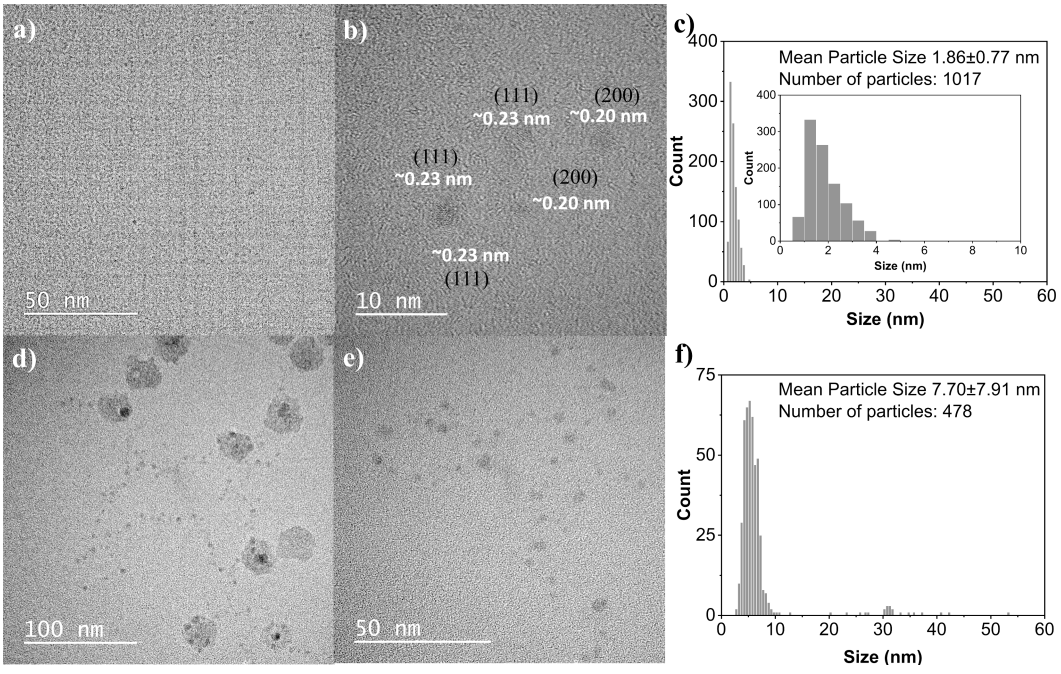


Figure 5. TEM images of NC8 (a, b) and NC11 (d, e) at different magnifications and the mean particle size distribution of AgNPs in NC8 (c) and NC11 (f).

follow a systematic decrease when the applied MWP decreases, attributed to less concentrated AgNP formation.

Although it is theoretically well-established that applying high MWP accelerates the heating rate and thus facilitates fast nanoparticle nucleation, the superheating can cause NP aggregation/fusion at extended reaction times.[29,33,35,36,43] Microwave energy can be transferred to the reaction medium via dipolar polarization, ionic conduction, and interfacial polarization,[44] and in a given solvent under flow conditions, superheating of the reaction mixture can be mitigated by decreasing the exposure time (increasing the flow rate) or the dissolved solute amounts (e.g., $AgNO_3$ and polymer) or both.

Considering that the highest absorbance intensity and the lowest PDI (~0.10) were obtained for AgNPs prepared at the MWP of 60 W (Figure 2c and Table 1), the effect of flow rate on the AgNP size and its distribution was evaluated at a constant MWP of 60 W. The flow rate effect was studied using 6 different combined flow rates. The flow rates of both pumps ($(0.25{:}0.25)_{NC11}$, $(0.50{:}0.50)_{NC10}$, $(0.75{:}0.75)_{NC3}$, $(1.00{:}1.00)_{NC9}$, $(1.25{:}1.25)_{NC8}$, $(1.50{:}1.50)_{NC7}$ mL/min) were simultaneously adjusted while the remaining experimental parameters (e.g., $AgNO_3$ concentration in DMSO, PCL concentration in DMF, and MWP) were kept constant (Table 1). At 60 W, the AgNP size decreased regularly when

https://doi.org/10.1021/acsomega.4c03612
ACS Omega 2025, 10, 18213−18224

Downloaded from pubs.acs.org/acsodf/article-pdf/10/18/18213/4082497/ao4c03612.pdf by guest on 26 October 2026

the flow rate increased. The color of produced NCs at 0.75:0.75, 1.00:1.00, 1.25:1.25, and 1.50:1.50 mL/min was transparent; however, it was gray at 0.50:0.50 and 0.25:0.25 mL/min (Figure 3a and Figure 2a for NC3). The UV−vis spectra of NC10 and NC11 displayed a broad absorption band at ca. 454 and 436 nm, and there was an additional absorption band at ca. 734 and 767 nm (Figure 3b) with fwhm's at ca. 480 nm, suggesting the presence of nonspherical NPs.[43,45,46] In contrast, the characteristic single UV−vis absorption band at ∼430 nm suggested spherical AgNPs forming at the flow rates of 1.50:1.50, 1.25:1.25, 1.00:1.00, and 0.75:0.75 mL/min (Figure 3b and Figure 2b for NC3). The UV−vis absorption maximum for the spherical AgNPs is generally reported at ca. 405−413 nm;[47] however, there are also studies reporting the absorption band for the small AgNPs at ca. 428 nm.[48,49] Although the HRTEM image of NC8 (see Figure 5) displays ultrasmall spherical AgNPs, the slight broadening in the absorption band may be attributed to the presence of some fused AgNPs (>50 nm) observed by HRTEM (SI Figure S3). Such NP fusing was also observed in previous studies under microwave-flow heating conditions.[33] The size of high-aspect-ratio AgNPs at a combined flow rate of 0.25:0.25 mL/min was 55.99 ± 4.79 nm (NC11), while the size of spherical ones at 1.50:1.50 mL/min (NC7) was 2.26 ± 0.15 nm (Table 1 and Figure 3c). A similar declining trend was observed in the PDI values when the flow rates increased from 0.25:0.25 mL/min (PDI ∼ 0.49) up to 1.25:1.25 mL/min (PDI ∼ 0.10) (Table 1). The PDI of ∼0.1 for NC8 suggested almost homogeneous nucleation and growth of AgNPs at 1.25:1.25 mL/min under 60 W of applied MWP. After 1.25:1.25 mL/min, the PDI at 1.50:1.50 mL/min for NC7 slightly increased to ∼0.31, suggesting a broadening in AgNP size distribution. Such PDI increase at 1.50:1.50 mL/min can be ascribed to the reduced microwave exposure time, which may cause ineffective nucleation and growth processes under high flow rates.[50−52] The transition from spherical to high-aspect-ratio AgNPs occurs almost after the flow rate of 0.75:0.75 mL/min. After the morphology change, a significant increase in the size of AgNPs is observed between spherical (3.24 ± 0.03 nm at 1.00:1.00 mL/min) and high-aspect-ratio (53.84 ± 0.98 nm at 0.50:0.50 mL/min) AgNPs. However, the size variation in the spherical AgNPs is minimal when the flow rate further increases to 1.25:1.25 mL/min (2.43 ± 0.62 nm) and 1.50:1.50 mL/min (2.26 ± 0.15 nm). Such a fast size change (∼17-fold) can be related to the microwave exposure time since the measured temperatures outside of the microwave zone are comparable at 0.50:0.50 mL/min (37.5 ± 2 °C) and 1.00:1.00 mL/min (35.5 ± 2 °C), suggesting that the size and morphology of AgNPs can be manipulated by only changing the flow rate in the MWFS.

The effect of flow rate under microwave-assisted continuous flow synthesis of AgNPs was previously studied for the particles produced at 4 mL/min (58.5 nm) and 8 mL/min (61.4 nm) flows.[53] In that study, a particle size increase (∼10%) was reported at a high flow rate. Similarly, we compared NC9 (1.00:1.00 mL/min) and NC10 (0.50:0.50 mL/min) as model systems. The DLS analysis of NC9 (∼3 nm) and NC10 (∼50 nm) displayed a particle size increase when the flow rate was nearly halved (Table 1). The gradual size increase was typical for all studied slow flows. In addition, it is worth noting that all studied experimental conditions yielded AgNPs with hydrodynamic sizes smaller than 3 nm at flow rates higher than 0.5:0.5 mL/min. Such an observed trend in particle size and its distribution can be attributed to the type of microwave source, in which a single-mode microwave[29,33−36] was used to prepare the NCs in the current study compared to a multimode domestic microwave (800 W) used in the former study.[53]

Overall, UV−vis spectroscopy and DLS results of NC7−11 showed that the optimum flow rate was 1.25:1.25 mL/min to prepare ultrasmall (2.43 ± 0.62) and almost monodisperse (PDI ∼ 0.1) AgNPs in the MWFS system.

Silver salt precursor concentration is another critical parameter when tuning the size, morphology, and distribution of AgNPs manufactured in the MWFS.[35,36,53] Therefore, a set of $AgNO_3$ concentrations in DMSO (0.02_{NC14}, 0.05_{NC13}, 0.10_{NC9}, and 0.20_{NC12} mg/mL) was studied at a combined flow rate of 1.00:1.00 mL/min under a constant MWP of 60 W and PCL concentration of 10 mg/mL. Transparent pale yellow solutions were obtained in all cases, and the yellow color intensity decreased gradually upon decreasing $AgNO_3$ concentrations (Figure 4a). Irrespective of $AgNO_3$ concentrations, a single UV−vis absorption band was observed at around 430−440 nm, attributable to spherical AgNPs (Figure 4b and Figure 3b for NC9). DLS analysis displayed a particle size increase when the $AgNO_3$ concentration was increased; however, the AgNP size was around 2 to 3 nm (Figure 4c, Table 1, and Figure 3c for NC9). The absorption band was intense at higher $AgNO_3$ concentrations, signifying increased AgNP concentration. The highest PDI was recorded for a 0.2 mg/mL concentration of $AgNO_3$, which could be related to a fast nucleation corroborated by the particle−particle interconnections at 60 W.[33]

In addition, polymer concentration affects the size and morphology of AgNPs in NCs, stabilizing NPs and preventing their further growth and aggregation.[35,36,54] Herein, the effect of PCL concentration was studied using 5.0_{NC15}, 10.0_{NC9}, and 20.0_{NC16} mg/mL PCL in DMF. The NC9 and NC16 were pale yellow transparent solutions; however, the color of NC15 was gray (Figure 4a and Figure 3a for NC9). At 5.0 mg/mL of PCL, two absorption bands positioned at ca. 426 and 673 nm are observed, suggesting rod-like AgNP formation.[43,45,46] A single UV−vis absorption band is obtained at 10.0 and 20.0 mg/mL concentrations of PCL (Figure 4b and Figure 3b for NC9). When the concentration of PCL increased to 20 mg/mL (NC16), the position of λ_{max} blue-shifted to ca. 411 nm compared to ca. 440 nm for NC9, indicating the presence of smaller AgNPs in the PCL.[35,54] DLS results of AgNPs (3.00 ± 0.22 nm) (Figure 4c) and the light yellow color of the NC16 (Figure 4a) agree well with the UV−vis absorption spectrum of NC16. In contrast, AgNP size becomes 8.82 ± 0.03 nm, three times bigger than NC9 (3.24 ± 0.03) and NC16, when 5 mg/mL of PCL was used (Figure 4c and Table 1).

TEM analysis of the selected NCs was performed to evaluate the size distribution, morphology, and crystallinity of the produced AgNPs. TEM samples were prepared using freshly prepared NC solutions. TEM images of NC8 (Figure 5a) and NC11 (Figure 5d,e) displayed spherical AgNPs with a mean size distribution of 1.86 ± 0.77 nm (Figure 5c) and 7.70 ± 7.91 nm (Figure 5f), respectively, and the results were in accord with DLS data (Table 1).

Further inspection of the TEM image of NC11 also showed large spherical NPs (∼20−40 nm) (Figure 5d,e), which increased the calculated mean particle size of AgNPs in NC11 (Figure 3f). The measured *d*-spacing of AgNPs in the HRTEM image of NC8 was approximately 0.23 and 0.20 nm (Figure

Downloaded from pubs.acs.org/acsodf/article-pdf/10/18/18213/4024975/ao4c03612.pdf by guest on 26 October 2026

https://doi.org/10.1021/acsomega.4c03612
ACS Omega 2025, 10, 18213−18224

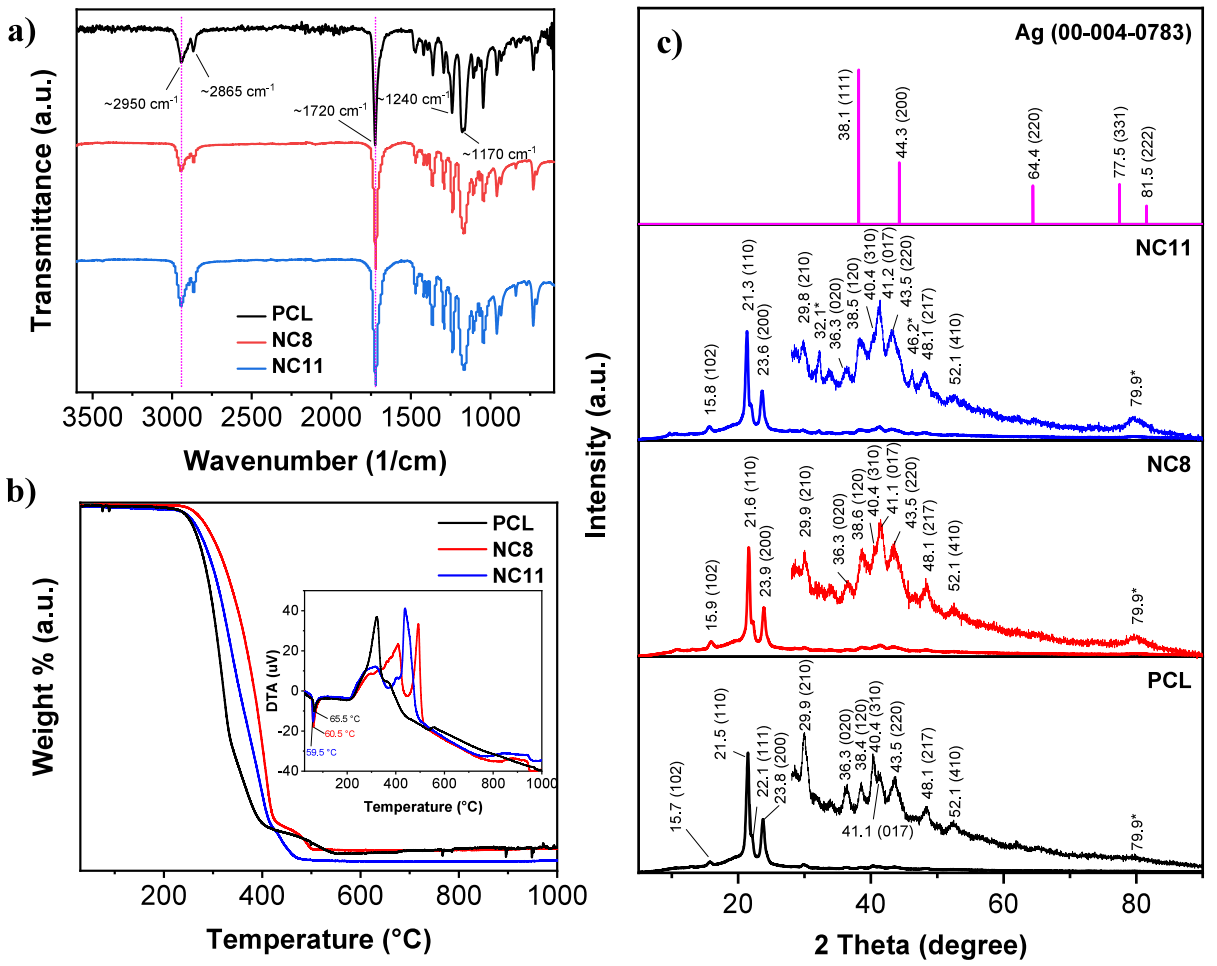


Figure 6. a) FTIR, b) TGA-DTA, and c) XRD results of PCL, NC8, and NC11. Inset in b shows the DTA vs temperature plot. Insets in c display the enlarged regions of corresponding PCL (black), NC8 (red), and NC11 (NC11). The labels correspond to the observed peak positions and diffraction planes.

5b), indicating AgNPs with (111) and (200) planes, respectively.[55] Furthermore, no silver oxide-based *d*-spacing was obtained in the analyzed TEM images, suggesting the effective stabilization of AgNPs by the PCL matrix.

ATR-FTIR spectroscopy was employed to assess the effect of AgNP incorporation on the characteristic vibrational modes of PCL. The FTIR spectra of PCL, NC8, and NC11 are given in Figure 6a, and the FTIR spectra of other NCs are presented in SI Figure S4a−d. The PCL displayed the characteristic carbonyl stretching (C═O) at ca. 1720 cm^{-1} and C−H stretchings at ca. 2950 and 2865 cm^{-1},[56] and the position of the bands was unchanged after composite formation. Unchanged peak positions can be associated with the absence of a chemical interaction between PCL and AgNP.[2]

The IR peaks at ca. 1170 and 1240 cm^{-1} were assigned to the symmetric and asymmetric C−O−C stretching bands, respectively.[57] The relative peak intensity (I) ratio of C═O and C−O−C bands ($I_{C-O-C}/I_{C=O}$) decreased upon AgNP incorporation. The $I_{C-O-C}/I_{C=O}$ of NC8 decreased by ∼18% compared to PCL, while the $I_{C-O-C}/I_{C=O}$ of NC11 is only ∼1%, suggesting a size-dependent physical interaction between PCL and AgNPs.

The thermal properties of NC8, NC11, and PCL were studied using TGA-DTA (Figure 6b). Additional TGA-DTA graphs for NC1−7, NC9−10, and NC12−14 are presented in SI Figure S5. As-received PCL started degradation at ca. 230 °C under air and displayed a three-step weight loss profile at ca. 310, 370, and 505 °C, agreeing with the PCL degradation under oxygen.[58] Embedding AgNPs in the PCL matrix shifted the degradation onset to ca. 240 and 250 °C for NC11 and NC8, respectively. Previous studies reported decreased degradation temperature when 10−20 nm AgNPs were loaded in a PCL/PEO[19] due to high thermal conductivity. In contrast, in our studies, the degradation onset decreased, ascribed to the homogeneous distribution of small-sized AgNPs (NC11:6.80 ± 6.01 nm, NC8:1.86 ± 0.77 nm) in the PCL matrix by the microwave-fluidic *in situ* manufacturing method. In addition, the three-step weight loss profile was conserved for NC8 and NC11, and the weight losses of NC8 were observed at ca. 350, 400, and 490 °C, while NC11 is at ca. 340, 390, and 440 °C. The DTA curve displayed a sharp endothermic peak, attributed to the melting point of PCL,[58] at ca. 65.5 °C; this peak shifted to 60.5 and 59.5 °C for NC8 and NC11, respectively, due to AgNPs embedding. The enhanced thermal stability of NC8, which contains smaller AgNPs (1.86 ± 0.77 nm) in the PCL matrix, can be due to the higher surface area to volume ratio of the smaller NPs. This leads to stronger interactions and better dispersion within the PCL matrix, effectively restricting polymer chain mobility and enhancing thermal stability. Additionally, smaller AgNPs promote more effective char formation during thermal degradation, which acts as a protective barrier. These factors, combined with better

Downloaded from pubs.acs.org/acsodf/article-pdf/10/18/18213/4082497/5/ao4c03612.pdf by guest on 26 October 2026

https://doi.org/10.1021/acsomega.4c03612
ACS Omega 2025, 10, 18213−18224

interaction with polymer chains and reduced agglomeration, contribute to the superior thermal stability observed in NC8.[59−62]

Changes in the crystallinity of PCL and the formation of AgNPs were monitored by XRD analysis. XRD patterns of PCL, NC8, NC11, and the simulated metallic AgNPs (JCPDs Card no. 004-0783) as comparison are shown in Figure 6c, and the XRD of NC1−7, NC9−10, and NC12−14 are presented in SI Figure S6. PCL displayed two intense diffraction peaks at ca. 21.5° and 23.8°, assigned to (110) and (200) planes in the crystal structure of the orthorhombic unit cell in PCL, respectively.[63−65] There were also weak signals at ca. 15.7°, 22.1°, 29.9°, 36.3°, 38.4°, 40.4°, 41.2° 43.5°, 48.1°, and 52.1° associated with the (102), (111), (210), (020), (120), (310), (017), (220), (217), and (410) planes, respectively.[65] The position of all observed diffraction peaks was unchanged; however, there were noticeable intensity changes in specific PCL-related peaks after AgNP incorporation. For instance, the intensity of the peaks at ca. 15.7° and 79.9° slightly increased while the peak intensity at ca. 29.9° decreased. Almost unchanged XRD peak positions and the slight peak intensity variations suggested that PCL crystallinity was not heavily dependent on AgNP incorporation.

Five characteristic diffraction peaks located at ca. 38.1°, 44.3°, 64.4°, 77.5°, and 81.5° and assigned to (111), (200), (220), (311), and (222) planes are expected for metallic AgNPs (JCPDs Card no. 00-004-0783) (Figure 6c).[35,66] However, less intense but sharp peaks localized mainly between 35° and 45° in the XRD pattern of the PCL[67] overlap with the expected intense AgNP diffractions (e.g., 38.1° and 44.3°) in this region (Figure 6c). Therefore, AgNPs in the NC8 and NC11 could not be monitored by XRD, although AgNP presence was affirmed by UV−vis and HR-TEM analyses. Furthermore, there were additional Bragg reflections at ca. 32.1° and 46.2° in the XRD pattern of NC11, attributed to silver oxide planes.[68] In contrast, no oxide formation was observed in the XRD of NC8, suggesting that the size of AgNPs in the PCL matrix is critical to preventing oxidation.

Antibacterial Activity of NCs. PCL, NC8, and NC11 films, prepared using the dip coating method, were assessed regarding their antibacterial activity against two Gram-positive bacteria (*S. aureus* and *P. aeruginosa*) and a Gram-negative bacterium (*E. coli*). Typically, the same size glass slides were dipped into the NC (or PCL) solution with 200 μL/min speed and retrieval with the same speed. The resultant dried films were characterized by ellipsometry (SI Figure S7). Information about film thickness, roughness, refractive index, and mean-squared error (MSE) of analyzed samples are summarized in Table 2.

The thickness, roughness, and refractive index of NC films increased after AgNP loading, and the increase was correlated with the size of AgNPs. Further, low MSE values suggested that the selected model (Cauchy film model) effectively calculated the films' thickness, roughness, and refractive index. The films were subjected to antibacterial activity tests, and the results are presented in Table 3.

Table 2. Ellipsometry Measurement Results of Samples for Antibacterial Tests

Sample	Thickness (nm)	Roughness (nm)	Refractive index (n)	MSE
PCL	85.73	3.95	1.416	1.29
NC8	106.27	5.28	1.505	2.459
NC11	133.51	9.21	1.501	0.875

Table 3. Antibacterial Activity of PCL, NC8, and NC11 Films against *E. coli*, *P. aeruginosa*, and *S. aureus*

Sample	*E. coli* (Gram-negative) (%)	*S. aureus* (Gram-positive) (%)	*P. aeruginosa* (Gram-negative) (%)
PCL	48.6	67.1	55.3
NC8	98.2	99.1	98.2
NC11	82.3	92.3	85.7

A substantial reduction in the number of viable bacteria was observed, and this fact was more outstanding in NC8-coated glasses, which showed the activity of 98.2% and 98.17% for *E. coli* (Gram-negative) and *P. aeruginosa* (Gram-negative), respectively (Figure 7). The activity toward *S. aureus* (Gram-positive) was higher than Gram-negative (~99.1%), agreeing with the literature.[69] The reason behind this is the thickness of the peptidoglycan layer, which primarily absorbs Ag ions into the bacterium, destroying bacteria. Since the thickness of this layer is higher in *S. aureus,* the bacterium sensitivity against Ag ion release is higher than the two others.[70] Furthermore, PCL-coated glasses did not exhibit a selective antibacterial effect on bacteria (Figure 7). Exposure of each bacterium to NC films decreased bacteria CFU. This decrease was more significant in NC8 with small AgNPs, which agrees with the previous findings.[71−73]

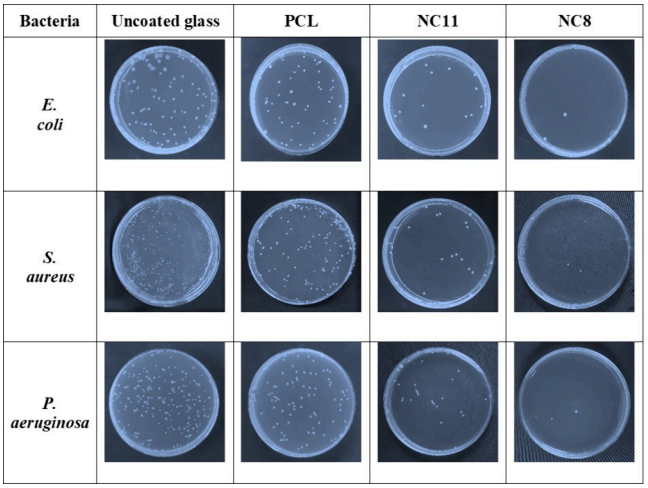


Figure 7. Colony-forming units (CFU) of *E. coli*, *S. aureus*, and *P. aeruginosa* after exposure to uncoated glass and PCL, NC8, and NC11 films.

The observed variation in antibacterial activity between NC8 and NC11 can be attributed to differences in the size and dispersity of the AgNPs. Although NC11 had a slower Ag/PCL flux, resulting in a higher concentration of AgNPs within the PCL matrix with higher film thickness, NC8 exhibited superior antibacterial properties. This is likely due to the smaller size and monodispersity of the AgNPs in NC8, which had an average size of approximately 1.86 ± 0.77 nm, as confirmed by UV−vis, DLS, and HR-TEM analyses. In contrast, NC11 contained larger AgNPs with an average size of 7.70 ± 7.91 nm. It is well-established in the literature that smaller NPs have a greater surface area-to-volume ratio, enhancing their

Downloaded from pubs.acs.org/acsodf/article-pdf/10/18/18213/4082497/5/ao4c03612.pdf by guest on 26 October 2026

https://doi.org/10.1021/acsomega.4c03612
ACS Omega 2025, 10, 18213−18224

interaction with bacterial cells and, thus, their antibacterial efficacy. Therefore, despite the higher concentration of AgNPs in NC11, the smaller, more uniformly distributed AgNPs in NC8 were more effective in inhibiting bacterial growth. These findings underscore the importance of AgNP size and dispersity in determining the antibacterial effectiveness of AgNP/PCL NCs.[72,74−77] The difference in antibacterial activity can be affected by the number of particles and their size.[35,36] Given the low concentration of AgNPs in NC8 (0.21%) compared to NC11 (0.55%) by ICP-OES, it can be deduced that small AgNPs have more unusual antibacterial activities when compared to larger counterparts.

CONCLUSION

A dual-injection microwave-fluidic reactor system can continuously manufacture US-AgNPs (1.86 ± 0.77 nm) in a biodegradable polymer matrix, PCL, under microwave-fluidic conditions without a reducing agent. Fine-tuning the MWP, flow rate, and precursor concentration controls the AgNP size and its distribution in the PCL matrix effectively at reaction temperatures below 50 °C and in less than 3 min of residence time. Embedding US-AgNPs in the PCL matrix increases the PCL degradation temperature onset by 20 °C. The PCL crystallinity is almost independent of the AgNP size and amount; however, NP incorporation increases NC films' roughness and refractive index. Antibacterial activity studies reveal that AgNP size is a dominating factor in antibacterial efficiency toward Gram-negative and Gram-positive bacteria compared to its amount. Overall, the presented continuous process brings a novel viewpoint to traditional polymer-based NC manufacturing, offering control over the fillers' size and distribution using an energy-efficient and almost green approach. It can be exploited to prepare other hybrid systems.

ASSOCIATED CONTENT

Supporting Information

The Supporting Information is available free of charge at https://pubs.acs.org/doi/10.1021/acsomega.4c03612.

Images of dried NCs, FTIR, TGA-DTA, XRD spectra for all NCs, and additional antibacterial test illustrations (PDF)

AUTHOR INFORMATION

Corresponding Author

Mustafa Kemal Bayazıt − *Sabancı University Nanotechnology Research and Application Center, İstanbul 34956, Turkey; Faculty of Engineering and Natural Science, Sabancı University, İstanbul 34956, Turkey;* orcid.org/0000-0002-3203-6601; Email: mkbayazit@sabanciuniv.edu

Authors

Mona Nejatpour − *Sabancı University Nanotechnology Research and Application Center, İstanbul 34956, Turkey*

Oğuz Bayındır − *Sabancı University Nanotechnology Research and Application Center, İstanbul 34956, Turkey;* orcid.org/0000-0003-2567-6157

Pelin Duru − *Faculty of Engineering and Natural Science, Sabancı University, İstanbul 34956, Turkey*

Milad Torabfam − *Faculty of Engineering and Natural Science, Sabancı University, İstanbul 34956, Turkey*

Cem Meriç − *Faculty of Engineering and Natural Science, Sabancı University, İstanbul 34956, Turkey*

Hasan Kurt − *School of Engineering and Natural Sciences and Research Institute for Health Sciences and Technologies (SABITA), Istanbul Medipol University, Istanbul 34810, Turkey; Nanosolar Plasmonics, Ltd., Kocaeli 41400, Turkey*

Meral Yüce − *Sabancı University Nanotechnology Research and Application Center, İstanbul 34956, Turkey; Faculty of Engineering and Natural Science, Sabancı University, İstanbul 34956, Turkey;* orcid.org/0000-0003-0393-1225

Complete contact information is available at: https://pubs.acs.org/10.1021/acsomega.4c03612

Notes

The authors declare the following competing financial interest(s): Patent pending (TR2021/011988, PCT/TR2022/050465) on the approach to manufacturing high-efficiency antimicrobial NCs reported herein continuously.

ACKNOWLEDGMENTS

This work is funded by the 2232 International Fellowship for Outstanding Researchers Program of TÜBİTAK (Grant 118C316). The funder had no role in the study design, data collection, analysis, the decision to publish, or the preparation of this article.

REFERENCES

(1) Huh, A. J.; Kwon, Y. J. "Nanoantibiotics": a new paradigm for treating infectious diseases using nanomaterials in the antibiotics resistant era. *J. Controlled Release* **2011**, *156* (2), 128−145.

(2) Tran, P. A.; Hocking, D. M.; O'Connor, A. J. In situ formation of antimicrobial silver nanoparticles and the impregnation of hydrophobic polycaprolactone matrix for antimicrobial medical device applications. *Mater. Sci. Eng. C Mater. Biol. Appl.* **2015**, *47*, 63−69.

(3) Neal, A. L. What can be inferred from bacterium-nanoparticle interactions about the potential consequences of environmental exposure to nanoparticles? *Ecotoxicology* **2008**, *17* (5), 362−371.

(4) Karwowska, E. Antibacterial potential of nanocomposite-based materials − a short review. *Nanotechnol. Rev.* **2017**, *6* (2), 243−254.

(5) Duncan, T. V. Applications of nanotechnology in food packaging and food safety: barrier materials, antimicrobials and sensors. *J. Colloid Interface Sci.* **2011**, *363* (1), 1−24.

(6) Sanchez-Lopez, E.; Gomes, D.; Esteruelas, G.; Bonilla, L.; Lopez-Machado, A. L.; Galindo, R.; Cano, A.; Espina, M.; Ettcheto, M.; Camins, A.; et al. Metal-Based Nanoparticles as Antimicrobial Agents: An Overview. *Nanomaterials (Basel)* **2020**, *10* (2), 292.

(7) Irfan, M.; Polonskyi, O.; Hinz, A.; Mollea, C.; Bosco, F.; Strunskus, T.; Balagna, C.; Perero, S.; Faupel, F.; Ferraris, M. Antibacterial, highly hydrophobic and semi transparent Ag/plasma polymer nanocomposite coating on cotton fabric obtained by plasma based co-deposition. *Cellulose* **2019**, *26* (16), 8877−8894.

(8) Raza, M. A.; Kanwal, Z.; Rauf, A.; Sabri, A. N.; Riaz, S.; Naseem, S. Size- and Shape-Dependent Antibacterial Studies of Silver Nanoparticles Synthesized by Wet Chemical Routes. *Nanomaterials (Basel)* **2016**, *6* (4), 74.

(9) Kraśniewska, K.; Galus, S.; Gniewosz, M. Biopolymers-Based Materials Containing Silver Nanoparticles as Active Packaging for Food Applications−A Review. *International Journal of Molecular Sciences* **2020**, *21* (3), 698.

(10) Ghazzy, A.; Naik, R. R.; Shakya, A. K. Metal−Polymer Nanocomposites: A Promising Approach to Antibacterial Materials. *Polymers* **2023**, *15* (9), 2167.

(11) Gong, H.; Zhang, K.; Dicko, C.; Bülow, L.; Ye, L. Ag−Polymer Nanocomposites for Capture, Detection, and Destruction of Bacteria. *ACS Applied Nano Materials* **2019**, *2* (3), 1655−1663.

(12) You, W.; Yu, W.; Zhou, C. Cluster size distribution of spherical nanoparticles in polymer nanocomposites: rheological quantification

Downloaded from pubs.acs.org/acsodf/article-pdf/10/18/18213/4082497/5/ao4c03612.pdf by guest on 26 October 2026

and evidence of phase separation. *Soft Matter* **2017**, *13* (22), 4088−4098.
(13) Lyutakov, O.; Kalachyova, Y.; Solovyev, A.; Vytykacova, S.; Svanda, J.; Siegel, J.; Ulbrich, P.; Svorcik, V. One-step preparation of antimicrobial silver nanoparticles in polymer matrix. *J. Nanopart. Res.* **2015**, *17* (3), DOI: 10.1007/s11051-015-2935-3.
(14) Alissawi, N.; Zaporojtchenko, V.; Strunskus, T.; Hrkac, T.; Kocabas, I.; Erkartal, B.; Chakravadhanula, V. S. K.; Kienle, L.; Grundmeier, G.; Garbe-Schönberg, D.; Faupel, F. Tuning of the ion release properties of silver nanoparticles buried under a hydrophobic polymer barrier. *J. Nanopart. Res.* **2012**, *14* (7), DOI: 10.1007/s11051-012-0928-z.
(15) Cameron, R. E.; Kamvari-Moghaddam, A. Synthetic bioresorbable polymers. *In Durability and Reliability of Medical Polymers* **2012**, 96−118.
(16) Mochane, M. J.; Motsoeneng, T. S.; Sadiku, E. R.; Mokhena, T. C.; Sefadi, J. S. Morphology and Properties of Electrospun PCL and Its Composites for Medical Applications: A Mini Review. *Applied Sciences* **2019**, *9* (11), 2205.
(17) Zhang, X.; Peng, X.; Zhang, S. W. Synthetic biodegradable medical polymers. *In Science and Principles of Biodegradable and Bioresorbable Medical Polymers* **2017**, 217−254.
(18) Deshmukh, K.; Basheer Ahamed, M.; Deshmukh, R. R.; Khadheer Pasha, S. K.; Bhagat, P. R.; Chidambaram, K. Biopolymer Composites With High Dielectric Performance: Interface Engineering. *In Biopolymer Composites in Electronics* **2017**, 27−128.
(19) Dubey, P.; Bhushan, B.; Sachdev, A.; Matai, I.; Uday Kumar, S.; Gopinath, P. Silver-nanoparticle-Incorporated composite nanofibers for potential wound-dressing applications. *J. Appl. Polym. Sci.* **2015**, *132* (35), DOI: 10.1002/app.42473.
(20) Yin, J.; Deng, B. Polymer-matrix nanocomposite membranes for water treatment. *J. Membr. Sci.* **2015**, *479*, 256−275.
(21) Diez-Pascual, A. M.; Luceno-Sanchez, J. A. Antibacterial Activity of Polymer Nanocomposites Incorporating Graphene and Its Derivatives: A State of Art. *Polymers (Basel)* **2021**, *13* (13), 2105.
(22) Xie, Z.; Zhang, P.; Zhang, Z.; Chen, C.; Wang, X. The choice of antimicrobial polymers: Hydrophilic or hydrophobic? *Chin. Chem. Lett.* **2024**, *35*, 109768.
(23) Sethy, N. K.; Arif, Z.; Mishra, P. K.; Kumar, P. Nanocomposite film with green synthesized TiO2 nanoparticles and hydrophobic polydimethylsiloxane polymer: synthesis, characterization, and antibacterial test. *Journal of Polymer Engineering* **2020**, *40* (3), 211−220.
(24) Si, Z.; Zheng, W.; Prananty, D.; Li, J.; Koh, C. H.; Kang, E. T.; Pethe, K.; Chan-Park, M. B. Polymers as advanced antibacterial and antibiofilm agents for direct and combination therapies. *Chem. Sci.* **2022**, *13* (2), 345−364.
(25) Borjihan, Q.; Dong, A. Design of nanoengineered antibacterial polymers for biomedical applications. *Biomater Sci.* **2020**, *8* (24), 6867−6882.
(26) Garcia, E. L.; Attallah, O. A.; Mojicevic, M.; Devine, D. M.; Brennan Fournet, M. Antimicrobial Active Bioplastics Using Triangular Silver Nanoplate Integrated Polycaprolactone and Polylactic Acid Films. *Materials* **2021**, *14* (5), 1132.
(27) Radhakrishnan, S.; Nagarajan, S.; Belaid, H.; Farha, C.; Iatsunskyi, I.; Coy, E.; Soussan, L.; Huon, V.; Bares, J.; Belkacemi, K.; et al. Fabrication of 3D printed antimicrobial polycaprolactone scaffolds for tissue engineering applications. *Materials Science and Engineering: C* **2021**, *118*, 111525.
(28) Dahal, N.; García, S.; Zhou, J.; Humphrey, S. M. Beneficial Effects of Microwave-Assisted Heating versus Conventional Heating in Noble Metal Nanoparticle Synthesis. *ACS Nano* **2012**, *6* (11), 9433−9446.
(29) Saleem, Q.; Torabfam, M.; Fidan, T.; Kurt, H.; Yüce, M.; Clarke, N.; Bayazit, M. K. Microwave-Promoted Continuous Flow Systems in Nanoparticle Synthesis—A Perspective. *ACS Sustainable Chem. Eng.* **2021**, *9* (30), 9988−10015.
(30) Dlugosz, O.; Banach, M. Inorganic nanoparticle synthesis in flow reactors - applications and future directions. *Reaction Chemistry & Engineering* **2020**, *5* (9), 1619−1641.
(31) Ching Lau, C.; Kemal Bayazit, M.; Reardon, P. J. T.; Tang, J. Microwave Intensified Synthesis: Batch and Flow Chemistry. *Chem. Rec.* **2019**, *19* (1), 172−187.
(32) Glasnov, T. N.; Kappe, C. O. Microwave-Assisted Synthesis under Continuous-Flow Conditions. *Macromol. Rapid Commun.* **2007**, *28* (4), 395−410.
(33) Bayazit, M. K.; Yue, J.; Cao, E.; Gavriilidis, A.; Tang, J. Controllable Synthesis of Gold Nanoparticles in Aqueous Solution by Microwave Assisted Flow Chemistry. *ACS Sustainable Chem. Eng.* **2016**, *4* (12), 6435−6442.
(34) Bayazit, M. K.; Cao, E.; Gavriilidis, A.; Tang, J. A microwave promoted continuous flow approach to self-assembled hierarchical hematite superstructures. *Green Chem.* **2016**, *18* (10), 3057−3065.
(35) Torabfam, M.; Nejatpour, M.; Fidan, T.; Kurt, H.; Yüce, M.; Bayazit, M. K. A microwave-powered continuous fluidic system for polymer nanocomposite manufacturing: a proof-of-concept study. *Green Chem.* **2022**, *24* (7), 2812−2824.
(36) Saleem, Q.; Torabfam, M.; Kurt, H.; Yüce, M.; Bayazit, M. K. Microwave-promoted continuous flow synthesis of thermoplastic polyurethane−silver nanocomposites and their antimicrobial performance. *Reaction Chemistry & Engineering* **2022**, *7* (7), 1510−1524.
(37) Ou, S.-F.; Huang, M.-S.; Chiou, S.-Y.; Ou, K.-L. Research of antibacterial activity on silver containing yttria-stabilized−zirconia bioceramic. *Ceram. Int.* **2013**, *39* (4), 3591−3596.
(38) Glor, E. C.; Ferrier, R. C.; Li, C.; Composto, R. J.; Fakhraai, Z. Out-of-plane orientation alignment and reorientation dynamics of gold nanorods in polymer nanocomposite films. *Soft Matter* **2017**, *13* (11), 2207−2215.
(39) Pastoriza-Santos, I. I.; Serra-Rodriguez, C.; Liz-Marzan, L. M. Self-Assembly of Silver Particle Monolayers on Glass from Ag(+) Solutions in DMF. *J. Colloid Interface Sci.* **2000**, *221* (2), 236−241.
(40) Pastoriza-Santos, I.; Liz-Marzán, L. M. Binary cooperative complementary nanoscale interfacial materials. Reduction of silver nanoparticles in DMF. Formation of monolayers and stable colloids. *Pure Appl. Chem.* **2000**, *72* (1−2), 83−90.
(41) Pastoriza-Santos, I.; Liz-Marzán, L. M. Formation and Stabilization of Silver Nanoparticles through Reduction by N,N-Dimethylformamide. *Langmuir* **1999**, *15* (4), 948−951.
(42) Jakab, A.; Rosman, C.; Khalavka, Y.; Becker, J.; Trügler, A.; Hohenester, U.; Sönnichsen, C. Highly Sensitive Plasmonic Silver Nanorods. *ACS Nano* **2011**, *5* (9), 6880−6885.
(43) Shibatani, A.; Matsumura, S.; Asakuma, Y.; Saptoro, A. Promoting Nucleation in Microwave-Assisted Nanoparticle Synthesis Using Combined Two-Stage Irradiation and Anti-Solvent Addition. *Crystal Research and Technology* **2019**, *54* (6), No. 1800205.
(44) Gude, V. G.; Patil, P.; Martinez-Guerra, E.; Deng, S.; Nirmalakhandan, N. Microwave energy potential for biodiesel production. *Sustainable Chemical Processes* **2013**, *1* (1), 5.
(45) Desai, R.; Mankad, V.; Gupta, S.; Jha, P. Size Distribution of Silver Nanoparticles: UV-Visible Spectroscopic Assessment. *Nanoscience and Nanotechnology Letters* **2012**, *4* (1), 30−34.
(46) Bindhu, M. R.; Umadevi, M. Silver and gold nanoparticles for sensor and antibacterial applications. *Spectrochim Acta A Mol. Biomol Spectrosc* **2014**, *128*, 37−45.
(47) Vu, X. H.; Duong, T. T. T.; Pham, T. T. H.; Trinh, D. K.; Nguyen, X. H.; Dang, V.-S. Synthesis and study of silver nanoparticles for antibacterial activity against Escherichia coli and Staphylococcus aureus. *Advances in Natural Sciences: Nanoscience and Nanotechnology* **2018**, *9* (2), No. 025019.
(48) Maneerung, T.; Tokura, S.; Rujiravanit, R. Impregnation of silver nanoparticles into bacterial cellulose for antimicrobial wound dressing. *Carbohydr. Polym.* **2008**, *72* (1), 43−51.
(49) Bustos-Guadarrama, S.; Nieto-Maldonado, A.; Flores-López, L. Z.; Espinoza-Gomez, H.; Alonso-Nuñez, G. Photocatalytic degradation of azo dyes by ultra-small green synthesized silver nanoparticles. *Journal of the Taiwan Institute of Chemical Engineers* **2023**, *142*, No. 104663.

Downloaded from pubs.acs.org/acsodf/article-pdf/10/18/18213/4082497/ao4c03612.pdf by guest on 26 October 2026

(50) Chikan, V.; McLaurin, E. J. Rapid Nanoparticle Synthesis by Magnetic and Microwave Heating. *Nanomaterials (Basel)* **2016**, *6* (5), 85.
(51) Thanh, N. T. K.; Maclean, N.; Mahiddine, S. Mechanisms of Nucleation and Growth of Nanoparticles in Solution. *Chem. Rev.* **2014**, *114* (15), 7610−7630.
(52) Kwon, S. G.; Hyeon, T. Formation Mechanisms of Uniform Nanocrystals via Hot-Injection and Heat-Up Methods. *Small* **2011**, *7* (19), 2685−2702.
(53) Dzido, G.; Jarzębski, A. B. Fabrication of silver nanoparticles in a continuous flow, low temperature microwave-assisted polyol process. *J. Nanopart. Res.* **2011**, *13* (6), 2533−2541.
(54) Wang, M.; Li, H.; Li, Y.; Mo, F.; Li, Z.; Chai, R.; Wang, H. Dispersibility and Size Control of Silver Nanoparticles with Anti-Algal Potential Based on Coupling Effects of Polyvinylpyrrolidone and Sodium Tripolyphosphate. *Nanomaterials (Basel)* **2020**, *10* (6), 1042.
(55) Xie, Z.-X.; Tzeng, W.-C.; Huang, C.-L. One-Pot Synthesis of Icosahedral Silver Nanoparticles by Using a Photoassisted Tartrate Reduction Method under UV Light with a Wavelength of 310 nm. *ChemPhysChem* **2016**, *17* (16), 2551−2557.
(56) Liu, M.; Luo, G.; Wang, Y.; He, W.; Liu, T.; Zhou, D.; Hu, X.; Xing, M.; Wu, J. Optimization and integration of nanosilver on polycaprolactone nanofibrous mesh for bacterial inhibition and wound healing in vitro and in vivo. *Int. J. Nanomedicine* **2017**, *12*, 6827−6840.
(57) Coates, J. Interpretation of Infrared Spectra, A Practical Approach. In *Encyclopedia of Analytical Chemistry*; Citeseer, 2006.
(58) Unger, M.; Vogel, C.; Siesler, H. W. Molecular weight dependence of the thermal degradation of poly(epsilon-caprolactone): a thermogravimetric differential thermal Fourier transform infrared spectroscopy study. *Appl. Spectrosc.* **2010**, *64* (7), 805−809.
(59) Hammani, S.; Barhoum, A.; Bechelany, M. Fabrication of PMMA/ZnO nanocomposite: effect of high nanoparticles loading on the optical and thermal properties. *J. Mater. Sci.* **2018**, *53* (3), 1911−1921.
(60) Jafarzadeh, S.; Jafari, S. M. Impact of metal nanoparticles on the mechanical, barrier, optical and thermal properties of biodegradable food packaging materials. *Crit Rev. Food Sci. Nutr* **2021**, *61* (16), 2640−2658.
(61) Aleksandrova, G. P.; Prozorova, G. F.; Klimenkov, I. V.; Sukhov, B. G.; Trofimov, B. A. Effect of metal nanoparticles on the thermal stability and conductivity of nanocomposites. *Bulletin of the Russian Academy of Sciences: Physics* **2016**, *80* (1), 49−54.
(62) Paul, D.; Paul, S.; Roohpour, N.; Wilks, M.; Vadgama, P. Antimicrobial, mechanical and thermal studies of silver particle-loaded polyurethane. *J. Funct Biomater* **2013**, *4* (4), 358−375.
(63) Alghamdi, A.; Alattas, H.; Saeed, W.; Al-Odayni, A.-B.; Ahmed, A.; Al-Owais, A.; Aouak, T. Thermal Properties, Isothermal Decomposition by Direct Analysis in Real-Time-of-Flight Mass Spectrometry and Non Isothermal Crystallization Kinetics of Poly(Ethylene-co-Vinyl Alcohol)/Poly(ε-Caprolactone) Blend. *Crystals* **2021**, *11* (3), 292.
(64) Baptista, C.; Azagury, A.; Shin, H.; Baker, C. M.; Ly, E.; Lee, R.; Mathiowitz, E. The effect of temperature and pressure on polycaprolactone morphology. *Polymer* **2020**, *191*, 122227.
(65) Bittiger, H.; Marchessault, R. H.; Niegisch, W. D. Crystal structure of poly-ε-caprolactone. *Acta Crystallographica Section B Structural Crystallography and Crystal Chemistry* **1970**, *26* (12), 1923−1927.
(66) Neelgund, G. M.; Hrehorova, E.; Joyce, M.; Bliznyuk, V. Synthesis and characterization of polyaniline derivative and silver nanoparticle composites. *Polym. Int.* **2008**, *57* (10), 1083−1089.
(67) Nanaki, S. G.; Papageorgiou, G. Z.; Bikiaris, D. N. Crystallization of novel poly(ε-caprolactone)-block-poly(propylene adipate) copolymers. *J. Therm. Anal. Calorim.* **2012**, *108* (2), 633−645.
(68) Jeung, D.-G.; Lee, M.; Paek, S.-M.; Oh, J.-M. Controlled Growth of Silver Oxide Nanoparticles on the Surface of Citrate Anion Intercalated Layered Double Hydroxide. *Nanomaterials* **2021**, *11* (2), 455.
(69) Jo, Y.; Garcia, C. V.; Ko, S.; Lee, W.; Shin, G. H.; Choi, J. C.; Park, S.-J.; Kim, J. T. Characterization and antibacterial properties of nanosilver-applied polyethylene and polypropylene composite films for food packaging applications. *Food Biosci* **2018**, *23*, 83−90.
(70) Jokar, M.; Rahman, R. A.; Ibrahim, N. A.; Abdullah, L. C.; Tan, C. P. Melt Production and Antimicrobial Efficiency of Low-Density Polyethylene (LDPE)-Silver Nanocomposite Film. *Food Bioprocess Tech* **2012**, *5* (2), 719−728.
(71) Osonga, F. J.; Akgul, A.; Yazgan, I.; Akgul, A.; Eshun, G. B.; Sakhaee, L.; Sadik, O. A. Size and Shape-Dependent Antimicrobial Activities of Silver and Gold Nanoparticles: A Model Study as Potential Fungicides. *Molecules* **2020**, *25* (11), 2682.
(72) Mtimet, I.; Lecamp, L.; Kebir, N.; Burel, F.; Jouenne, T. Green synthesis process of a polyurethane-silver nanocomposite having biocide surfaces. *Polym. J.* **2012**, *44* (12), 1230−1237.
(73) Hung, H.-S.; Hsu, S.-h. Biological performances of poly(ether)-urethane−silver nanocomposites. *Nanotechnology* **2007**, *18* (47), 475101.
(74) Osonga, F. J.; Akgul, A.; Yazgan, I.; Akgul, A.; Eshun, G. B.; Sakhaee, L.; Sadik, O. A. Size and shape-dependent antimicrobial activities of silver and gold nanoparticles: A model study as potential fungicides. *Molecules* **2020**, *25* (11), 2682.
(75) Liu, H.-L.; Dai, S. A.; Fu, K.-Y.; Hsu, S.-h. Antibacterial properties of silver nanoparticles in three different sizes and their nanocomposites with a new waterborne polyurethane. *International Journal of Nanomedicine* **2010**, *5*, 1017−1028.
(76) Yin, I. X.; Zhang, J.; Zhao, I. S.; Mei, M. L.; Li, Q.; Chu, C. H. The antibacterial mechanism of silver nanoparticles and its application in dentistry. *International Journal of Nanomedicine* **2020**, *Volume 15*, 2555−2562.
(77) Menichetti, A.; Mavridi-Printezi, A.; Mordini, D.; Montalti, M. Effect of size, shape and surface functionalization on the antibacterial activity of silver nanoparticles. *Journal of Functional Biomaterials* **2023**, *14* (5), 244.

Downloaded from pubs.acs.org/acsodf/article-pdf/10/18/18213/4082497/5/ao4c03612.pdf by guest on 26 October 2026

https://doi.org/10.1021/acsomega.4c03612
ACS Omega 2025, 10, 18213−18224